



Infrared and terahertz studies of phase transitions in the  $\text{CH}_3\text{NH}_3\text{PbBr}_3$  perovskiteV. Železný <sup>\*</sup>, C. Kadlec , and S. Kamba *Institute of Physics, Academy of Sciences of the Czech Republic Na Slovance 2, 182 20 Prague 8, Czech Republic*D. Repčák *Institute of Physics, Academy of Sciences of the Czech Republic Na Slovance 2, 182 20 Prague 8, Czech Republic  
and Faculty of Nuclear Sciences and Physical Engineering, Czech Technical University in Prague,  
Břehová 7, 115 19 Prague 1, Czech Republic*S. Kundu  and M. I. Saidaminov *Department of Chemistry, University of Victoria, Victoria, BC, V8W 2Y2, Canada*

(Received 1 March 2023; revised 3 May 2023; accepted 10 May 2023; published 25 May 2023)

We investigated the influence of two structural phase transitions in methylammonium lead tri-bromide  $\text{CH}_3\text{NH}_3\text{PbBr}_3$  ( $\text{MAPbBr}_3$ ) single crystals on the activity of polar phonons using time-domain THz transmission and far infrared (IR) reflectance spectra. The fitting using the Lorentz model of damped harmonic oscillators also enables us to determine all the polar phonon parameters, IR response functions, and their temperature dependence. The fit of the far IR spectra provides a nearly perfect quantitative description of the measured reflectance at room temperature using three phonons. On cooling, three IR active phonons of the cubic and tetragonal structures split into 15 separate bands, signaling the transformation to the orthorhombic phase below 150 K. This result is compared with the factor group analysis of the polar phonons in all three crystallographic phases. The absence of a soft optical phonon supports the previously published order-disorder character of the structural phase transitions.

DOI: [10.1103/PhysRevB.107.174113](https://doi.org/10.1103/PhysRevB.107.174113)

## I. INTRODUCTION

Organic-inorganic hybrid lead-halide perovskites  $\text{MAPbX}_3$  ( $X=\text{Br}, \text{Cl}, \text{I}$ ) have attracted a lot of attention in recent years due to their outstanding properties in potential applications such as photovoltaic cells, light-emitting diodes and lasers, and photodetectors [1–4]. They excel in high power conversion efficiency (exceeding 24%), low manufacturing cost, and are exceptional for their key parameters such as large diffusion length [5–7], long charge lifetime [8,9], high carrier mobility [10,11], large absorption coefficient [12], and direct band gap [13,14]. Their properties are extremely interesting and very prospective for the solar cell industry if their durability and water resistance is improved, but that seems to be a surmountable problem [15,16].

The  $\text{ABX}_3$  perovskite structure of these materials consists of two subsystems: (i) a framelike sublattice of corner-sharing  $\text{PbX}_6$  octahedra on the  $B$  and  $X$  positions and (ii) MA (methylammonium)  $\text{CH}_3\text{NH}_3$  cations on the  $A$  perovskite position occupying cuboctahedral cages formed by surrounding octahedra.  $\text{MAPbBr}_3$  occurs in three crystal phases. At high temperatures, it is cubic  $Pm\bar{3}m$ , at  $T_{c1} = 236$  K undergoes a phase transition to a tetragonal phase  $I4/mcm$  and below  $T_{c2} = 150$  K transforms into an orthorhombic structure  $Pnma$  [17–21]. The structure is soft (its Young modulus being low)

and the two high-temperature phases show an orientational disorder due to the random orientation of the MA cations. The phase transition sequence and the temperature variation of the lattice parameters have been published using synchrotron x-ray powder diffraction [22]. In addition, between the tetragonal and orthorhombic phases in temperature interval 149–155 K, another intermediate incommensurate phase has been found [23].

The dielectric measurements ( $10^2$ – $10^{11}$  Hz), ultrasonic velocity and attenuation at 10 MHz, and Raman scattering in the temperature interval 100–300 K have been reviewed [24], suggesting large dipolar disorder of the MA cations resulting in high dielectric constant  $\epsilon_{\text{stat}} = 58$  below 1 GHz in the cubic phase. The disorder continuously reduces with decreasing temperature. A minimum of the ultrasonic velocity observed at 236 K is caused by a ferroelastic phase transition to tetragonal phase and its steep increase below 149 K and the steep decrease in the permittivity indicates an order-disorder transition in the MA system during the phase transition to orthorhombic phase. Another review on disorder in  $\text{MAPbX}_3$  compounds including different experimental techniques and their comparison is in Ref. [25].

The generation and transport of free carriers in  $\text{MAPbBr}_3$  are strongly influenced by electron-phonon coupling, which modifies their transport properties and effective mass. THz and far IR (FIR) spectroscopies represent very suitable techniques to provide useful information on lattice phonons, dynamic MA modes, and their interactions with their

<sup>\*</sup>zelezny@fzu.cz

environment. The FIR spectra of the  $\text{MAPbX}_3$  family have already been measured but are mostly limited to room temperature and transmission of thin films. The most recent and complete studies have been published and reviewed in several papers [26–28]. The authors [26] reported on the vibrational eigenmodes and eigenfrequencies assignment, their density functional calculation, and factor-group analysis in the orthorhombic  $Pnma$  phase at 10 K. They show that the IR spectrum consists of three contributions: the internal vibration of the MA cations, their librations and external vibrations, and phonons of the  $\text{PbBr}_3$  network. Room-temperature transmittance and reflectance were used to study strong anharmonicity and dynamic disorder in  $\text{MAPbX}_3$  thin films and single crystals [27]. Room-temperature FIR reflectance [28] was measured to study the  $\text{MAPbBr}_3$  single crystals and three IR-active phonon modes were found fitting the spectrum between 40 and  $200\text{ cm}^{-1}$ . The time-domain THz spectroscopy was carried out on  $\text{MAPbBr}_3$  at various temperatures [29,30].

In this paper, we present the results of the measurement of the FIR reflectance in the frequency range  $30$  to  $650\text{ cm}^{-1}$  and the time-domain THz transmission in the low frequency region ( $10$ – $60\text{ cm}^{-1}$ ) of pure  $\text{MAPbBr}_3$  single crystals at temperatures ranging from  $10$  to  $300\text{ K}$ . We use the combination of the two techniques because they show clear and smooth spectra and, using the fitting procedure, we determine the parameters of the vibrational modes and their temperature dependence, especially at structural phase transitions. The number of the observed polar phonons is compared with the prediction of factor-group analysis in the different  $\text{MAPbBr}_3$  crystal structures. At room temperature, we also present the IR reflectance and transmittance from  $400$  to  $4000\text{ cm}^{-1}$ , revealing the internal polar vibrations of the MA molecule.

## II. EXPERIMENTAL

$40\text{ wt } \%$  methylamine and  $48\%$  HBr solutions in  $\text{H}_2\text{O}$ , and  $\text{PbBr}_2$  ( $\geq 98\%$ ) were purchased from Sigma-Aldrich. Dimethylformamide (DMF) was purchased from Fisher Scientific. All chemicals were used without further purification.

Methylammonium bromide (MABr) was synthesized following standard procedure.  $86.4\text{ mL}$  of the methylamine solution was added to a  $4\text{ L}$  round bottom flask in an ice bath and then  $1000\text{ mL}$  of  $95\%$  ethanol was added. Then  $118.8\text{ mL}$  of the HBr solution was slowly added with a dripping funnel with continuous stirring over an hour. After complete addition, the mixture was stirred for other  $2\text{ h}$  to maximize the yield. Then the solvent was evaporated. The remaining solid was dissolved in a minimum amount of boiling ethanol. After complete dissolution, the solution was left overnight for crystallization. The white MABr solid crystals were filtered out and washed with diethylether and dried under vacuum for more than  $24\text{ h}$ .

The  $\text{MAPbBr}_3$  crystals were grown by a modified inverse temperature crystallization reported previously [31]. The growth solution was prepared by dissolving  $1.4\text{ M}$   $\text{PbBr}_2$  and  $1.43\text{ M}$  MABr in DMF overnight with continuous stirring. The solution was left undisturbed for  $12\text{ h}$  and then was filtered to a crystallizing dish by  $0.45\text{ }\mu\text{m}$  PVDF syringe filters before crystallization. The hot plate temperature was set to  $36\text{ }^\circ\text{C}$ . A plastic was wrapped and ten holes were made

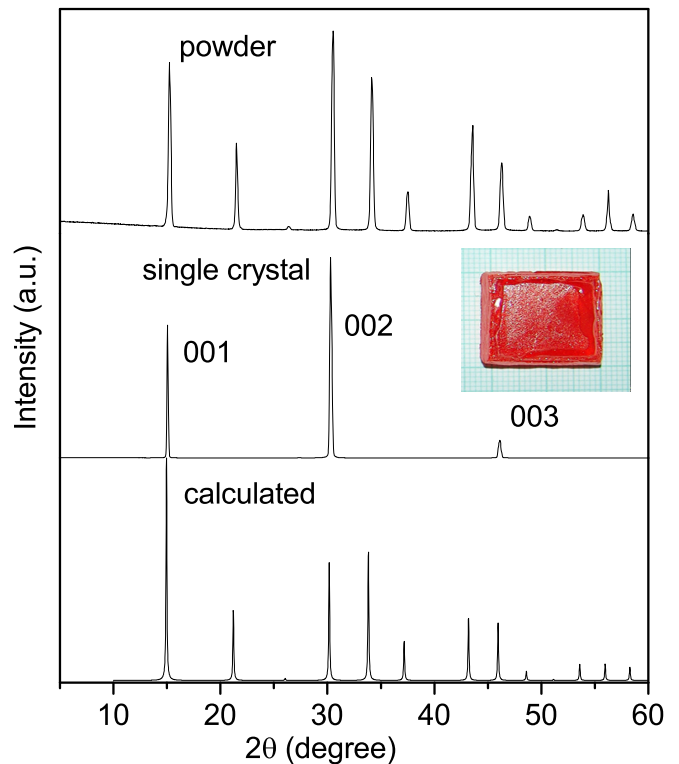


FIG. 1. X-ray diffraction patterns of the  $\text{MAPbBr}_3$  at room temperature for powder, single crystal, and calculated powder sample. The cubic  $Pm\bar{3}m$  space group assignment is used. Inset shows a photo of one of our crystals.

with a needle to enable slow evaporation. The temperature of the hot plate was slowly increased to  $41\text{ }^\circ\text{C}$  with a rate of  $0.5\text{ }^\circ\text{C/h}$  and then it was left overnight for crystallization. A crystal seed started to grow and the temperature of the hot plate was increased slowly to  $45\text{ }^\circ\text{C}$ , with  $2\text{ }^\circ\text{C/day}$  rate. The temperature was kept at  $45\text{ }^\circ\text{C}$  for  $2\text{ days}$ . Finally, a large size crystal of  $20 \times 20 \times 5\text{ mm}^3$  was harvested. The samples for our experiments were cut from the crystal, ground to needed thickness, and polished to have optical lustre.

The orientation of the  $\text{MAPbBr}_3$  single crystal was checked by measuring the x-ray diffraction from its surface using a PANalytical Empyrean system equipped with a  $\text{Cu K}\alpha$  ( $\lambda = 1.5406\text{ \AA}$ ) source. The diffraction patterns are shown in Fig. 1 with peaks localized at  $14.879^\circ$ ,  $30.484^\circ$  and  $45.853^\circ$  corresponding to (001), (002), and (003) crystal planes, respectively.

The room-temperature IR reflectance at a near-normal angle of incidence was measured over a wide frequency range between  $30$  and  $4000\text{ cm}^{-1}$  with a metallic mirror as a reference. The room-temperature middle-IR (MIR) transmittance, which was limited by the sample transparency, was measured in a range  $400$ – $4000\text{ cm}^{-1}$  using an empty aperture as a reference. The spectra were taken from the  $(100)_c$  cubic surface of  $\text{MAPbBr}_3$  crystals of the size  $10 \times 8 \times 2\text{ mm}^3$  and an aluminum mirror was used as a reference. The crystal for MIR transmittance measurement was  $655\text{ }\mu\text{m}$  thick. A Fourier transform spectrometer Bruker IFS 113v equipped with pyroelectric DTGS detectors, globar and Hg radiation sources and KBr and broadband Mylar beamsplitters was used to cover the

MIR and FIR region, respectively. The temperature-dependent FIR reflectance (10–300 K) was measured in a range from 30 to 650  $\text{cm}^{-1}$ . The samples were placed in an Optistat CF Oxford Instrument He-flow cryostat and the signal was detected by a Si bolometer operating at 1.6 K.

A custom-made time-domain THz-transmission spectrometer is used to determine the complex transmission function of a 100- $\mu\text{m}$ -thick crystal from 10 to 60  $\text{cm}^{-1}$  (0.3–2 THz). The train of femtosecond pulses generated by a Ti-sapphire laser oscillator (Coherent, Mira) produces linearly polarized broadband THz pulses in a photoconducting switch TeraSED (Giga-Optics). A gated detection scheme based on electro-optic sampling with a 1-mm-thick [110] ZnTe crystal as a sensor allows us to measure the time profile of the electric field of the transmitted THz pulse. The time-dependent signal is Fourier-transformed to a complex transmission function, which is numerically inverted into complex refractive index and THz reflectivity is calculated.

In order to better understand the nature of the phonons active in the FIR spectral range and to determine their parameters, we fit the merged reflectivity with the following formula

$$R(\omega) = \left| \frac{\sqrt{\tilde{\epsilon}(\omega)} - 1}{\sqrt{\tilde{\epsilon}(\omega)} + 1} \right|^2, \quad (1)$$

where the complex dielectric function,  $\tilde{\epsilon}(\omega)$ , is modeled by the Lorentz formula, consisting of the sum of  $n$  damped harmonic oscillators representing polar optic phonons

$$\tilde{\epsilon}(\omega) = \epsilon_1(\omega) + i\epsilon_2(\omega) = \epsilon_\infty + \sum_{j=1}^n \frac{\omega_{Pj}^2}{\omega_{TOj}^2 - \omega^2 - i\omega\gamma_j}, \quad (2)$$

where  $\omega_{TOj}$ ,  $\omega_{Pj}$ , and  $\gamma_j$  are the transverse resonance frequency, so-called phonon plasma frequency, and damping of the  $j$ th IR-active phonon.  $\epsilon_\infty$  is the contribution of all optical active transitions at higher frequencies. The static permittivity is given by the sum of IR-active phonons and electronic contributions,

$$\epsilon(0) = \epsilon_\infty + \epsilon_{ph} = \epsilon_\infty + \sum_{j=1}^n \frac{\omega_{Pj}^2}{\omega_{TOj}^2} = \epsilon_\infty + \sum_{j=1}^n \Delta\epsilon_j, \quad (3)$$

where  $\Delta\epsilon_j = \omega_{Pj}^2/\omega_{TOj}^2$  is the contribution of the  $j$  mode to static  $\epsilon(0)$ , sometimes also called the phonon dielectric strength. In this way, IR spectroscopy provides a useful estimate of static dielectric permittivity if we do not assume any dielectric relaxations below the phonon frequencies.

### III. RESULTS AND DISCUSSION

All spectra in this paper are taken from the (100)<sub>c</sub> surface plane of MAPbBr<sub>3</sub> single crystals. The unpolarized radiation is used because of the crystal optical isotropy in the room-temperature cubic phase and the indefinite orientation of the tetragonal/orthorhombic domain structure in low-temperature phases. In this case, all optic-active phonons are observed independently of their polarization.

The experimental MIR reflectance and transmittance from 400 to 4000  $\text{cm}^{-1}$  at room temperature are presented in Fig. 2.

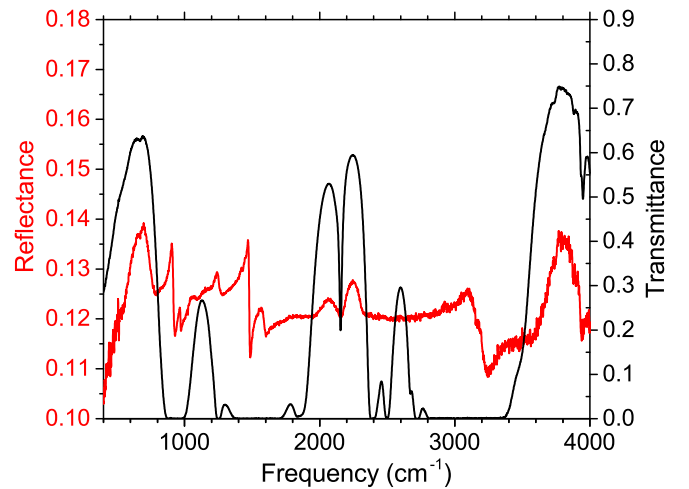


FIG. 2. Room-temperature MIR reflectance of 2-mm-thick MAPbBr<sub>3</sub> single crystal and transmittance of 655- $\mu\text{m}$ -thin slab.

The transmittance spectra show three broad regions of high transmission at 700, 2200, and 3800  $\text{cm}^{-1}$  and two smaller ones. They correspond to the bands of similar shapes at the same frequencies in reflectance that are results of the incoherent reflection from the sample rear surface. Besides these features, several other sharper reflectance peaks can be seen in the spectrum originating from the internal MA molecule vibrations having maxima near 905, 965, 1242, 1422, 1467, and 1568  $\text{cm}^{-1}$ , and a broad band at 3100  $\text{cm}^{-1}$ . The weak spectral features at 3050, 3100, and 3170  $\text{cm}^{-1}$  can be resolved from the asymmetric peak profile. The frequencies of all these peaks do not very much differ from the values of its derivative published in Refs. [26,32,33] and can be interpreted in the same way as done by those authors. Their measurements were carried out at 10 K, therefore, their peaks are sharper than ours. Anyway, we can approximately estimate at room temperature 9 of 12 internal vibrations observed by them at 10 K [26].

In the FIR region, we restrict ourselves to reflectance spectra because the material is nontransparent in this interval due to the strong absorption related to phonons, which hinders the transmission measurements except using very thin films. As the FIR signal below 30  $\text{cm}^{-1}$  is weak due to Hg lamp source, the FIR reflectance from 30 to 650  $\text{cm}^{-1}$  is merged with the reflectivity calculated from the time-domain THz transmission data below 60  $\text{cm}^{-1}$ . The resulting spectra significantly vary with temperature as displayed in Fig. 3, where the spectra are cut off at 400  $\text{cm}^{-1}$  because the reflectance is completely flat (no dispersion) at higher FIR frequencies.

The room-temperature FIR reflectance displays a broad reststrahlen band below 200  $\text{cm}^{-1}$  and another sharper maximum at 45  $\text{cm}^{-1}$ . It reminds us in some aspects of the broad spectra of classical oxide perovskites, however, it is compressed to lower frequencies. This indicates smaller oscillator strengths of the participating phonons in comparison to the classical oxide perovskites [34]. The RT reflectance spectrum with respect to its shape and intensity level is in good agreement with the room-temperature spectra in Refs. [27,28]. Using Eqs. (1) and (2), it can be decomposed into three IR-active

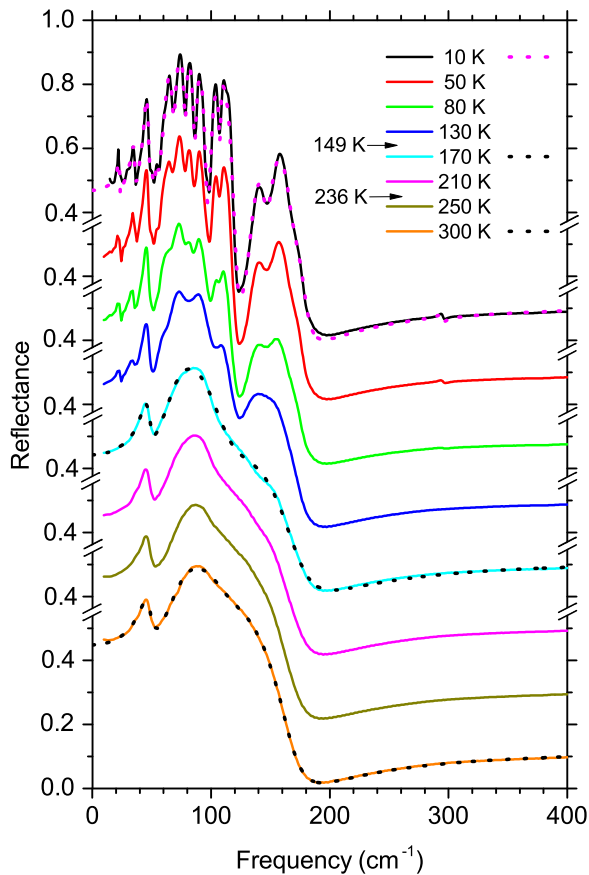


FIG. 3. Merged FIR reflectance and calculated THz reflectivity of MAPbBr<sub>3</sub> single crystal at various temperatures. The reflectance spectra in the graph are shifted with decreasing temperature by 0.2 along the y axis. The arrows indicate phase transition temperatures. The dots show the fits in all three crystal phases at 300, 170, and 10 K.

modes and their parameters are given in Table I. There are some deviations between the phonon parameters obtained in Ref. [28] and our data that can be explained by the different formula used for  $\tilde{\epsilon}(\omega)$  in Ref. [28] and by us. The origin of the spectral features comes from the vibrations of the PbBr<sub>3</sub> frame and the contributions from the external (librational and translational) motion of MA molecules [26,33]. They can, in some approximation, also be interpreted in a similar way as the classical perovskites. The strongest mode with the highest plasma frequency in oxide perovskites, the so-called Slater mode, expresses the vibrations of *B* cations against *X* octahedra (Pb against Br anions) is in our case at 73 cm<sup>-1</sup>. The mode near 45 cm<sup>-1</sup>, the so-called last mode, presents the *A* atom

TABLE I. Room-temperature phonon parameters obtained from the optimum reflectance fit by the Lorentz model with  $\epsilon_{\infty} = 4.3$ .

No. <i>j</i>	$\omega_{TOj}$ (cm <sup>-1</sup> )	$\omega_{Pj}$ (cm <sup>-1</sup> )	$\gamma_j$ (cm <sup>-1</sup> )	$\Delta\epsilon_j$
1	45.6	116.6	10.7	6.5
2	73.2	273.1	26.9	13.9
3	117.6	102.1	56.8	0.8

vibrations against the rest of the crystal cell, where the entire MA molecule is considered as an effective atom. The highest frequency mode seen at 120 cm<sup>-1</sup> is the so-called Axe mode and is a deformation mode of PbBr<sub>6</sub> octahedra. Note that the Axe mode frequency is about 400 cm<sup>-1</sup> lower than that in oxide perovskites like SrTiO<sub>3</sub> or BaTiO<sub>3</sub> [34].

Figure 3 shows the temperature dependence of the merged FIR reflectance and calculated THz reflectivity. It clearly demonstrates the narrowing of the bands and the increase of their number and intensity with decreasing temperature. Such behavior results from the reduction of the phonon damping and the splitting of the original bands into several bands with lower plasma frequency. In addition to the above-mentioned temperature variation of the spectral bands, it is also possible to trace their changes when temperature passes across the phase transitions. The changes are very small at the 236 K phase transition and only a weak modulation appears in the spectrum below this temperature, caused mainly by the reduction of the mode damping. This radically changes at 150 K, where the spectral features narrow abruptly down and several new bands suddenly appear. This clearly indicates the existence of a structural phase transition. On the other hand, there is no spectral band shifting that would indicate the phonon softening typical for the displacive mechanism, when temperature approaches the phase transition. The observed behavior is characteristic for order-disorder-type phase transitions. Our results thus are in good agreement with the microwave dielectric measurement [24], where a weak anomaly for the 236 K transition and the order-disorder type for the 150 K phase transition are reported.

The merged THz and FIR reflectance at various temperatures is fit using Eqs. (1) and (2) to determine the phonon parameters. The fitting also allows us to compute all useful response functions. In the previous works [27,28], the authors used for their spectra fitting the generalized Lyddane-Sachs-Teller formula, sometimes also called the four-parameter factorized form or the Gervais model. This model is very convenient for highly ionic materials with large LO-TO splitting, i.e., with large oscillator strength, where the damping,  $\gamma(\omega)$ , as a function of  $\omega$  is different at  $\omega_{TO}$  and  $\omega_{LO}$  frequencies. Here, we prefer to use the classical Lorentz model, Eqs. (1) and (2), which can be used in the entire temperature range and is also suitable for the spectra characterized by sharp and narrow bands in reflectivity due to their small oscillator strength, which is exactly the case we have at low temperatures. Since unpolarized radiation is used for our reflectance measurement, the contributions of all IR active phonons are observed in the spectra independently of their selection rules. The comparison of the selected experimental and fit curves is also in Fig. 3. At 10 K, we obtain very rich FIR spectrum, which contains in total 15 phonons. Their parameters (frequency, oscillator strength, and damping) are listed in Table II. When all atoms in the orthorhombic crystal phase are considered, as has been done [26,32,33], 144 vibrational modes must be taken into account: 72 intramolecular, 24 translational and librational, and 48 of PbBr<sub>3</sub> frames of them 29 are IR active in FIR. We see in FIR only some of them (15 modes). It is because some of them overlap and are difficult to resolve. The parameters of our room-temperature modes are in reasonable agreement with those presented earlier [27,28].



TABLE II. Phonon parameters obtained from the optimum merged reflectance fit by the Lorentz model at 10 K with  $\epsilon_\infty = 4.2$ .

No. $j$	$\omega_{\text{TO}j}$ ( $\text{cm}^{-1}$ )	$\omega_{\text{P}j}$ ( $\text{cm}^{-1}$ )	$\gamma_j$ ( $\text{cm}^{-1}$ )	$\Delta\epsilon_j$
1	22.8	28.8	1.7	1.6
2	35.1	56.3	2.6	2.6
3	45.1	109.5	2.5	5.9
4	50.1	52.1	3.9	1.1
5	54.5	46.8	2.7	0.7
6	62.3	179.1	4.2	8.2
7	70.1	102.6	3.6	2.2
8	79.1	53.6	2.6	0.5
9	87.3	52.2	3.4	0.4
10	100.0	72.5	5.1	0.5
11	107.8	24.9	2.0	0.1
12	135.1	104.5	11.6	0.6
13	150.0	62.2	11.4	0.2
14	171.3	31.0	19.7	0.1
15	295.0	22.6	2.7	0.1

Comparing our spectra with the already published time-domain THz results [29,30], a reasonable agreement can be seen at low frequencies, where we also observe modes approximately at 35, 45, 60, and 70  $\text{cm}^{-1}$ . At higher frequencies, the coincidence is worse, first of all, due to the high noise in their spectra. Looking at the smoothness of our spectra and their coherent temperature development, we see a certain advantage in our spectra, which allows us to resolve more phonons. An interesting point is the practically perfect correspondence of our experimental RT reflectance with the RT model reflectivity shown in Ref. [30].

The temperature development of the real and imaginary part of the dielectric function and energy-loss function ( $-\text{Im}[1/\tilde{\epsilon}(\omega)]$ ) in all three phases is displayed in Fig. 4. It demonstrates even more lucidly the phonons' behavior with decreasing temperature: narrowing of the phonon bands and appearance of new phonons, but only small shifts of their frequencies. It also illustrates the small variation of the spectra at the cubic-tetragonal phase transition near 236 K and quite substantial changes below 150 K in the orthorhombic phase. Three phonons can be distinguished in the cubic and tetragonal phases and 15 phonons are identified in the orthorhombic phase at 10 K. Further details on the generation of new phonons in the whole temperature range are shown in Fig. 5, where the phonons are represented by their transverse frequencies ( $\omega_{\text{TO}j}$ ).

Additional information is provided by the energy-loss function, ( $-\text{Im}[1/\tilde{\epsilon}(\omega)]$ ), whose maxima are at the longitudinal phonon frequencies ( $\omega_{\text{LO}j}$ ) defined as the zeros of the dielectric function.  $\omega_{\text{LO}j}^2 = \omega_{\text{TO}j}^2 + \omega_{\text{P}j}^2/\epsilon_s$ , where the screened  $\epsilon_s$  is equal to  $\epsilon_\infty$  plus the sum of  $\Delta\epsilon_i$  of the phonons whose  $\omega_{\text{TO}i} > \omega_{\text{TO}j}$ . A very small change in the position of ( $\omega_{\text{LO}j}$ ) at both phase transitions means that the original oscillator strength of the high-temperature phase is distributed among the new split modes in the low-temperature phases.

The different behavior of our spectra at both phase transitions is also in agreement with the study of the thermal expansion of the lattice parameters and unit cell volume [22]. They

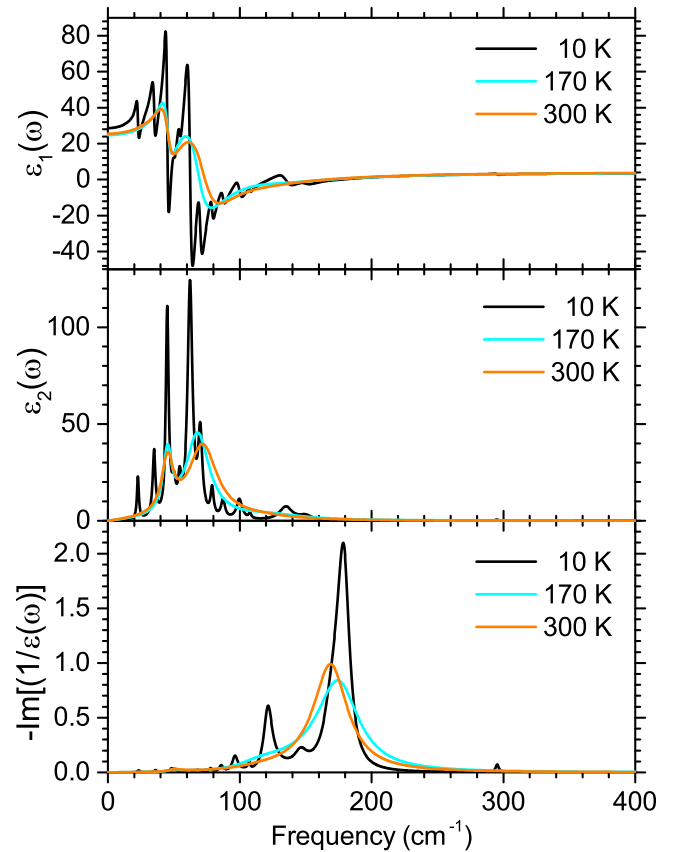
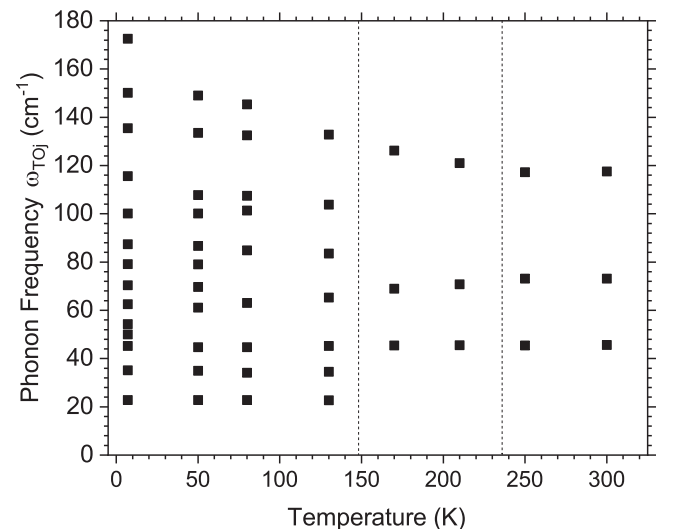


FIG. 4. Real and imaginary parts of dielectric function and energy-loss function in all three phases at selected temperatures 300, 170, and 10 K calculated from the optimal fit parameters.

vary linearly in the whole low-temperature orthorhombic phase and have an abrupt step at the orthorhombic-tetragonal phase transition typical for the first-order phase transition. Afterwards, they linearly continue to the phase transition at


 FIG. 5. Temperature dependence of the transverse phonon frequencies,  $\omega_{\text{TO}j}$ , obtained by the fit procedure. The dash lines depict the phase transition temperatures at 149 and 236 K.

236 K, where they have a very slight anomaly compatible with a second-order phase transition.

As mentioned above, the structure of MAPbBr<sub>3</sub> consists of two interpenetrating subsystems: the regular crystal structure of PbBr<sub>6</sub> octahedra and MA molecules. As the low symmetry of the MA molecule is incompatible with the crystal site symmetry, they exhibit no long-range orientational order. The phase transitions change the shape and size of the cuboctahedron cage and, thus, influence the dynamical behavior of the MA molecule. At high temperatures, they have no preferred orientations and they vibrate around a local equilibrium and jump between adjacent equilibrium positions reminding discrete plastic crystals. As temperature approaches the cubic-to-tetragonal transition, an antiferrodistortive rotation of PbBr<sub>6</sub> octahedra appears described by the (*a*<sup>0</sup>*a*<sup>0</sup>*c*<sup>-</sup>) Glazer classification [35,36]. The phase transition is similar to that of SrTiO<sub>3</sub> except for the complexity due to MA molecule occupying the perovskite *A* site. The tetragonal phase can be explained by the softening of the IR inactive transverse optic phonon (octahedron rotation) at the *R* point at the Brillouin zone boundary [37]. This is the reason why no noticeable changes are observed in the IR spectra or the dielectric data across the 236 K phase transition [24]. The coupling between the tilting angle and lattice strain leads to the elongation in the *c*-axis direction and softening of the *c*<sub>44</sub> elastic constant typical for the second-order phase transition into an improper ferroelastic phase [38].

In the orthorhombic *Pnma* phase, the molecular motion is completely frozen up, the molecules are orientationally ordered and a regular molecular crystal is formed with the (*a*<sup>+</sup>*b*<sup>-</sup>*b*<sup>-</sup>) octahedra tilting pattern. The tilting can be related to the simultaneous condensation of the rotational modes in the *R* and *M* points at the Brillouin zone boundary [37]. The phase transition is characterized by the large microwave dielectric anomaly and it is of the first order [24]. As to its character is considered of a order-disorder nature. This picture is in good agreement with our data because the low-frequency value for  $\epsilon(0) \sim 25$  from Eq. (3) is in good agreement with their high-frequency value in the microwave region and there is also good agreement with other measurements [39].

The lattice dynamics of MAPbBr<sub>3</sub> is dramatically different from traditional semiconductors, insulators, and even classical oxide perovskites. The cubic lattice constant is 5.926 Å for MAPbBr<sub>3</sub> in comparison to 3.905 Å for SrTiO<sub>3</sub>. The MA molecules are located at the center of very symmetrical cuboctahedron and have a lot of space for their motion. Their positions are well ordered in contrast to their rotation orientation. Their interactions with surrounding Br atoms due to van der Waals forces and hydrogen bondings [25] restrict their motion to the tumbling between the symmetry equivalent positions. The relatively free rotation motion resulting in dynamic local disorder allows these materials to be considered as discrete plastic crystals [40]. As to its symmetry, the MA molecules do not fit the site symmetry of the lattice and the high-temperature phases must be thought as pseudocubic. The total crystal structure including PbBr<sub>6</sub> and MA molecules is very soft and the interaction of the reorientational motion with the crystal elasticity allows the structure to be easily deformable.

Comparing our experimental data with several reports on the temperature dependence of Raman scattering in MAPbBr<sub>3</sub> [39,41–43], there are some similarities. The authors also found broad spectral features at room temperature which become narrower and split at low temperature. Their number, however, does not agree with the prediction of group analysis as our data do, and the frequencies of the phonon do not coincide with ours, but it is explainable because all three phases have centers of symmetry, so the selection rules for IR and Raman activity are different. Some authors claim that the low-temperature orthorhombic phase is ferroelectric [44], but, in this case, the structure should be noncentrosymmetric and the phonon activities in IR and Raman spectra should be the same, which we cannot confirm. They also claim to observe spectral features that characterize the *P4/mmm* phase between 150 and 155 K, which we do not observe. On the other hand, the mode splitting observed in Raman scattering is in qualitative agreement with our data.

The factor-group analysis has been primarily done for MAPbI<sub>3</sub>, which is isomorphic with MAPbBr<sub>3</sub> [26,33]. The five atoms (one of them a pseudoatom representing the MA molecule) in the unit cell of the *Pm* $\bar{3}$ *m* structure contribute to  $3F_{1u} + F_{2u}$  optical and  $F_{1u}$  acoustic modes. The real MA molecule cannot be classified by the  $F_{1u}$  irreducible representation because the molecule symmetry is lower than the symmetry of the perovskite *A* site. Its translation and libration modes, however, contribute to FIR spectrum. A similar situation comes in the tetragonal *I4/mcm* phase, where two MA molecules are replaced with two pseudoatoms that give  $A_{2u} + B_{2g} + E_g + E_u$  representations corresponding to the vibration modes on the perovskite *A* site. In the *Pnma* structure, the MA molecule symmetry ( $C_{3v}$ ) is higher than the crystal site symmetry ( $C_s$ ) and the molecule regularly builds into the crystal lattice. The orientation of the MA molecule is fixed regarding to PbBr<sub>3</sub> octahedra, the site occupancy by the C and N atoms of the MA cation is 1.0 and the molecule symmetry correlates with the site symmetry [25]. In this phase, MAPbBr<sub>3</sub> is transformed in a molecular crystal. It allows a correct and complete classification of all degrees of freedom [26,33] and the mode assignment. Further details on reduction to irreducible representations for all three phases are given in Appendix.

Using the results of the factor-group analysis, it is possible to find a way to qualitatively understand our FIR reflectance spectra. In the cubic phase, our fit resolves three phonons in comparison to two predicted by the group analysis assuming only the PbBr<sub>3</sub> structure. This can be improved by adding an effective mass point representing the MA cation that gives an additional  $F_{1u}$  optic mode. The same selection rules are then obtained as for classical cubic SrTiO<sub>3</sub>. The MA libration modes are mixed in the spectrum and along with the MA molecule disorder contribute to the spectral broadening. In the reflectance spectra of the tetragonal phase, there are only three phonons observed. The symmetry analysis for the tetragonal PbBr<sub>3</sub> network predicts six ( $2A_{2u} + 4E_u$ ) IR-active optic and three acoustic modes, and again the same selection rules as for tetragonal SrTiO<sub>3</sub> are obtained. The translation and libration modes of the MA molecule again contribute to FIR spectrum. The difference between the experiment and theory can be explained as in the foregoing case. Moreover, the

cubic-tetragonal phase transition is caused by the condensation of the  $R$  modes at the Brillouin zone boundary. These modes cannot be observed in FIR and also the anomaly in dielectric permittivity is very small. In the low-temperature orthorhombic phase, the fitting procedure resolves 15 phonons. The complete symmetry [33] predicts 20 IR-active optic modes of the  $\text{PbBr}_3$  network and three acoustic ones. In addition, five translation and four libration external FIR-active modes are expected. Such an amount of modes assuming their overlapping and broadening in experimental spectra is very difficult to resolve. What can be seen in the spectra is not a classical mode splitting due to a symmetry lowering. As temperature is decreasing, the dynamical and static disorder is reducing and the orientation of the MA molecule adjusts to be compatible with the crystal site symmetry. Finally, the crystal transforms in a nearly classical molecular crystal with a spectrum typical for this kind of crystal.

#### IV. CONCLUSIONS

Single crystals of  $\text{MAPbBr}_3$  grown by a modified in-verse temperature crystallization method, were studied by IR and THz spectroscopic techniques. Clear reflectance spectra were obtained in a broad spectral ( $10\text{--}3500\text{ cm}^{-1}$ ) and temperature range ( $10\text{--}300\text{ K}$ ) across all main crystal phases. Using the fitting procedure, their phonon parameters were determined in broad spectral and temperature regions and all important response functions were obtained. From their temperature dependence, we could identify two phase transitions. We discuss the dynamics that drives the phase transitions in  $\text{MAPbBr}_3$  and compare it to that in classical oxide perovskites. The two phase transitions are of quite different natures. The improper ferroelastic transition at  $236\text{ K}$  occurs at the  $R$  point of the Brillouin zone and very weakly changes the IR and dielectric spectra. The absence of optical soft mode and formation of many new phonons indicates a large contribution of the order-disorder mechanism to the phase transition at  $150\text{ K}$ . Our results are in agreement with previously published microwave dielectric spectra [24] and x-ray diffraction data [22].

#### ACKNOWLEDGMENTS

This work has been supported by the Czech Science Foundation (Project No. 21-06802S), the MŠMT Project SOLID 21-CZ.02.1.01/0.0/0.0/16\_019/0000760, and Grant Agency of the Czech Technical University in Prague (Project No. SGS22/182/OHK4/3T/14).

#### APPENDIX

##### 1. Tilted octahedra in perovskites

All three crystal phases can be realized by tilting  $\text{PbBr}_6$  octahedra. According to the Glazer classification [35,36], the tilts rotating around the crystal axes in phase are marked by + and, for out-of-phase, superscript. The cubic phase above  $236\text{ K}$  [ $Pm\bar{3}m$  ( $O_h^h$ ), space group NO. 221] has no tilt  $\mathbf{a}^0\mathbf{a}^0\mathbf{a}^0$ . The antiferrodistortive transition into the tetragonal phase

[ $I4/mcm$  ( $D_{4h}^{18}$ ), space group No. 140] with the alternating rotation mode along the  $c$  axis and tetragonally elongated in the same direction is described by  $\mathbf{a}^0\mathbf{a}^0\mathbf{c}^-$ . The orthorhombic phase [ $Pnma$  ( $D_{2h}^{16}$ ) space group No. 62] is denoted by  $\mathbf{a}^+\mathbf{b}^-\mathbf{b}^-$ , meaning an in-phase tilt around the [100] direction and antiphase tilts around the [010] and [001] directions. The space group  $Pnma$  is not a subgroup of  $I4/mcm$ , therefore no order parameter is possible to find describing the second-order phase transition between them. The phase transition between the tetragonal and orthorhombic phases is also complicated because of the incommensurately modulated phase between  $149$  and  $155\text{ K}$  which has been observed in Ref. [23]. There is, however, still some doubt about the influence of modulation or twinning on interpretation of the structural data.

##### 2. Factor group analysis

Here we review and complete the group analysis for all three crystal phases. We restrict the analysis to the  $\text{PbBr}_3$  framework, excluding the MA cations because of their disorder which vanished only in the orthorhombic phase. Above  $236\text{ K}$ , the cubic  $Pm\bar{3}m$  ( $O_h^h$ ) structure contains one formula unit in the primitive cell ( $Z = 1$ ). The acoustic modes have symmetry  $F_{1u}$  and the optic modes can be classified:

$$\underbrace{2F_{1u}}_{\text{IR active}} + \underbrace{F_{2u}}_{\text{silent}}$$

The tetragonal structure belongs to the  $I4/mcm$  ( $D_{4h}^{18}$ ) space group with two chemical formulas in the primitive cell of the body-centered tetragonal lattice (the cell is doubled,  $Z = 2$ ) and four formula units in the conventional (quadruple) cell. Its acoustic modes are represented by  $A_{2u} + E_u$  and the optic phonons are divided among

$$\underbrace{2A_{2u} + 4E_u}_{\text{IR active}} + \underbrace{A_{1g} + B_{1g} + B_{2g} + 2E_g}_{\text{Raman active}} + \underbrace{A_{1u} + B_{1u} + 2A_{2g}}_{\text{silent}}$$

The low-temperature orthorhombic phase  $Pnma$  ( $D_{2h}^{16}$ ) has four formula units in the primitive cell ( $Z = 4$ ). Its acoustic modes have irreducible representations  $B_{1u} + B_{2u} + B_{3u}$  as has been already shown and discussed in Ref. [33] for the orthorhombic phase:

$$\underbrace{7B_{1u} + 6B_{2u} + 7B_{3u}}_{\text{IR active}} + \underbrace{5A_g + 4B_{1g} + 5B_{2g} + 4B_{3g}}_{\text{Raman active}} + \underbrace{7A_u}_{\text{silent}}$$

The isolated MA molecule has ( $C_{3v}$ ) symmetry which is lower than the  $O_h$  or  $D_{4h}$  symmetry of the  $A$  site in cubic or tetragonal phases of the perovskite structure, respectively. If the molecule symmetry group is lower than the site symmetry group, it is not possible to use the correlation between them. This is the reason why the long-range ordering breaks and the structural disorder of the discrete plastic crystals is introduced. The 18 internal degrees of freedom of the MA molecule must be classified separately using  $5A_1 + A_2 + 6E$  irreducible representations of the isolated molecule, and its internal modes are observed in the middle IR spectral region. Six external degrees (librational and translational) contribute to the low-frequency FIR spectra in conjunction with the  $\text{PbBr}_3$  structure phonons. The case when the MA molecules are ordered as in the  $Pnma$  phase has been analyzed by Schuck *et al.* [33].

- [1] A. Y. Alsalloum, B. Turedi, X. Zheng, S. Mitra, A. A. Zhumeckenov, K. J. Lee, P. Maity, I. Gereige, A. AlSaggaf, I. S. Roqan *et al.*, *ACS Energy Lett.* **5**, 657 (2020).
- [2] Z. Chen, B. Turedi, A. Y. Alsalloum, C. Yang, X. Zheng, I. Gereige, A. AlSaggaf, O. F. Mohammed, and O. M. Bakr, *ACS Energy Lett.* **4**, 1258 (2019).
- [3] M. Grätzel, *Nat. Mater.* **13**, 838 (2014).
- [4] M. A. Green, A. Ho-Baillie, and H. J. Snaith, *Nat. Photonics* **8**, 506 (2014).
- [5] Q. Dong, Y. Fang, Y. Shao, P. Mulligan, J. Qiu, L. Cao, and J. Huang, *Science* **347**, 967 (2015).
- [6] D. Shi, V. Adinolfi, R. Comin, M. Yuan, E. Alarousu, A. Buin, Y. Chen, S. Hoogland, A. Rothenberger, K. Katsiev *et al.*, *Science* **347**, 519 (2015).
- [7] S. D. Stranks, G. E. Eperon, G. Grancini, C. Menelaou, M. J. Alcocer, T. Leijtens, L. M. Herz, A. Petrozza, and H. J. Snaith, *Science* **342**, 341 (2013).
- [8] C. Wehrenfennig, G. E. Eperon, M. B. Johnston, H. J. Snaith, and L. M. Herz, *Adv. Mater.* **26**, 1584 (2014).
- [9] Y. Bi, E. M. Hutter, Y. Fang, Q. Dong, J. Huang, and T. J. Savenije, *J. Phys. Chem. Lett.* **7**, 923 (2016).
- [10] Y. Zhang, Y. Liu, Y. Li, Z. Yang, and S. F. Liu, *J. Mater. Chem. C* **4**, 9172 (2016).
- [11] T. Baikie, N. S. Barrow, Y. Fang, P. J. Keenan, P. R. Slater, R. O. Piltz, M. Gutmann, S. G. Mhaisalkar, and T. J. White, *J. Mater. Chem. A* **3**, 9298 (2015).
- [12] Z. Lian, Q. Yan, Q. Lv, Y. Wang, L. Liu, L. Zhang, S. Pan, Q. Li, L. Wang, and J.-L. Sun, *Sci. Rep.* **5**, 16563 (2015).
- [13] A. Kojima, K. Teshima, Y. Shirai, and T. Miyasaka, *J. Am. Chem. Soc.* **131**, 6050 (2009).
- [14] W. S. Yang, J. H. Noh, N. J. Jeon, Y. C. Kim, S. Ryu, J. Seo, and S. I. Seok, *Science* **348**, 1234 (2015).
- [15] Z. Li, B. Li, X. Wu, S. A. Sheppard, S. Zhang, D. Gao, N. J. Long, and Z. Zhu, *Science* **376**, 416 (2022).
- [16] X. Zhao, T. Liu, Q. C. Burlingame, T. Liu, R. Holley, G. Cheng, N. Yao, F. Gao, and Y.-L. Loo, *Science* **377**, 307 (2022).
- [17] H. Mashiyama, Y. Kurihara, and T. Azetsu, *J. Korean Phys. Soc.* **32**, 156 (1998).
- [18] H. Mashiyama, Y. Kawamura, and Y. Kubota, *J. Korean Phys. Soc.* **51**, 850 (2007).
- [19] H. Mashiyama, Y. Kawamura, H. Kasano, T. Asahi, Y. Noda, and H. Kimura, *Ferroelectrics* **348**, 182 (2007).
- [20] F. Brivio, J. M. Frost, J. M. Skelton, A. J. Jackson, O. J. Weber, M. T. Weller, A. R. Goñi, A. M. A. Leguy, P. R. F. Barnes, and A. Walsh, *Phys. Rev. B* **92**, 144308 (2015).
- [21] C. A. López, M. V. Martínez-Huerta, M. C. Alvarez-Galván, P. Kayser, P. Gant, A. Castellanos-Gomez, M. T. Fernández-Díaz, F. Fauth, and J. A. Alonso, *Inorg. Chem.* **56**, 14214 (2017).
- [22] F. Lehmann, A. Franz, D. M. Töbrens, S. Levenco, T. Unold, A. Taubert, and S. Schorr, *RSC Adv.* **9**, 11151 (2019).
- [23] D. Wiedemann, J. Breternitz, D. W. Paley, and S. Schorr, *J. Phys. Chem. Lett.* **12**, 2358 (2021).
- [24] I. Anusca, S. Balčiūnas, P. Gemeiner, Š. Svirskas, M. Sanlıalp, G. Lackner, C. Fettkenhauer, J. Belovickis, V. Samulionis, M. Ivanov *et al.*, *Adv. Energy Mater.* **7**, 1700600 (2017).
- [25] J.-W. Lee, S. Seo, P. Nandi, H. S. Jung, N.-G. Park, and H. Shin, *iScience* **24**, 101959 (2021).
- [26] M. A. Pérez-Osorio, R. L. Milot, M. R. Filip, J. B. Patel, L. M. Herz, M. B. Johnston, and F. Giustino, *J. Phys. Chem. C* **119**, 25703 (2015).
- [27] M. Sendner, P. K. Nayak, D. A. Egger, S. Beck, C. Müller, B. Epding, W. Kowalsky, L. Kronik, H. J. Snaith, A. Pucci *et al.*, *Mater. Horiz.* **3**, 613 (2016).
- [28] J. Wang, E. Motaharifar, L. N. Murthy, M. Higgins, D. Barrera, T. B. Daunis, Y. Zheng, A. V. Malko, F. Ely, M. Quevedo-Lopez *et al.*, *J. Appl. Phys.* **125**, 025706 (2019).
- [29] D. Zhao, J. M. Skelton, H. Hu, C. La-o-vorakiat, J.-X. Zhu, R. A. Marcus, M.-E. Michel-Beyerle, Y. M. Lam, A. Walsh, and E. E. M. Chia, *Appl. Phys. Lett.* **111**, 201903 (2017).
- [30] M. Nagai, T. Tomioka, M. Ashida, M. Hoyano, R. Akashi, Y. Yamada, T. Aharen, and Y. Kanemitsu, *Phys. Rev. Lett.* **121**, 145506 (2018).
- [31] S. Kundu, J. O'Connell, A. Hart, D. Richtsmeier, M. Bazalova-Carter, and M. I. Saidaminov, *Adv. Electron. Mater.* **8**, 2200640 (2022).
- [32] T. Glaser, C. Müller, M. Sendner, C. Krekeler, O. E. Semonin, T. D. Hull, O. Yaffe, J. S. Owen, W. Kowalsky, A. Pucci *et al.*, *J. Phys. Chem. Lett.* **6**, 2913 (2015).
- [33] G. Schuck, D. M. Töbrens, M. Koch-Müller, I. Efthimiopoulos, and S. Schorr, *J. Phys. Chem. C* **122**, 5227 (2018).
- [34] J. Hlinka, J. Petzelt, S. Kamba, D. Noujni, and T. Ostapchuk, *Phase Transit.* **79**, 41 (2006).
- [35] A. M. Glazer, *Acta Crystallogr., Sect. B: Struct. Crystallogr. Cryst. Chem.* **28**, 3384 (1972).
- [36] C. J. Howard and H. T. Stokes, *Acta Crystallogr., Sect. B* **54**, 782 (1998).
- [37] R. C. Powell, *Symmetry, Group Theory, and the Physical Properties of Crystals* (Springer, New York, 2010).
- [38] J. Even, M. Carignano, and C. Katan, *Nanoscale* **8**, 6222 (2016).
- [39] M. Maczka and M. Ptak, *Solids* **3**, 111 (2022).
- [40] K. Miyata, T. L. Atallah, and X.-Y. Zhu, *Sci. Adv.* **3**, e1701469 (2017).
- [41] A. M. Leguy, A. R. Goñi, J. M. Frost, J. Skelton, F. Brivio, X. Rodríguez-Martínez, O. J. Weber, A. Pallipurath, M. I. Alonso, M. Campoy-Quiles *et al.*, *Phys. Chem. Chem. Phys.* **18**, 27051 (2016).
- [42] R. G. Niemann, A. G. Kontos, D. Palles, E. I. Kamitsos, A. Kaltzoglou, F. Brivio, P. Falaras, and P. J. Cameron, *J. Phys. Chem. C* **120**, 2509 (2016).
- [43] K. Nakada, Y. Matsumoto, Y. Shimoi, K. Yamada, and Y. Furukawa, *Molecules* **24**, 626 (2019).
- [44] Z.-R. Gao, X.-F. Sun, Y.-Y. Wu, Y.-Z. Wu, H.-L. Cai, and X. S. Wu, *J. Phys. Chem. Lett.* **10**, 2522 (2019).